Research Article

Dual Independent Rotor Axial Flux Induction Motor for Electric Vehicle Applications

Alireza Hesari (iD), **Ahmad Darabi** (iD), **and Fazel Pourmirzaei Deylami** (iD)

Faculty of Electrical Engineering, Shahrood University of Technology, Shahrood P.O. Box 3619995161, Iran

Correspondence should be addressed to Fazel Pourmirzaei Deylami; f.p.deylami@gmail.com

This article proposes a dual independent rotor axial flux induction motor (DIR-AFIM) with two degrees of freedom as a propulsion motor for an electric vehicle (EV). The performance of this motor in different operating conditions of the vehicle is discussed and investigated. This motor has two rotors that are mechanically independent of each other, providing driving force for the EV separately and enabling the removal of any mechanical or electrical differential. The propulsion motor can play the role of differential and also reduce the cost and complexity of the entire propulsion system in some extent. The finite element modeling of the proposed motor has been performed and the performance characteristics have been evaluated in three operating scenarios: flat path, sloped path, and turning path, taking into account the dynamics of the vehicle. Additionally, the accuracy of the simulations and modeling has been confirmed by performing some practical tests on the prototype machine. The results show that the simulations and measurements are in good agreement and the proposed propulsion system can be a suitable option for lightweight electric vehicles.

1. Introduction

Environmental problems caused by air pollution and excessive consumption of fossil fuels have caused attention to clean energy. The emission of harmful gases plays a significant role in creating these problems. It is estimated that about 27% of all harmful gas emissions are related to internal combustion vehicles (ICV) and transportation systems [1]. Due to the progress in the field of battery technology and the need to reduce the emission of harmful gases in recent years, electric vehicles (EVs) have attracted everyone's attention and this issue is considered as one of the effective ways to solve this problem. Compared to ICV, zero harmful gas emissions, more efficiency, and less noise and vibrations are among the advantages of EVs [2]. One of the most important parts of a vehicle is its drive, which is referred to as the heart of the vehicle. The drive system and powertrain as well as its response to vehicle load changes play a very important role in vehicle stability. In many working modes of the vehicle, such as moving on a straight path and a sloping path, the speed and torque of the driving wheels are the same. But in some other work modes such

as rotation (steering) or driving wheels under uneven friction on the road such as ice load, the driving wheels must rotate at different speeds. Also, for the stability of the vehicle, the torque of the drive wheels must be different. Therefore, there is a need for a system that manages the proper distribution of drive output torque between the driving wheels. The mechanical differential (final drive in the powertrain) is responsible for this task and transmits and divides the drive power and the torque into two flows between the wheels on the same axle in ICV. In EVs, the need for such a system is necessary for the stability of the vehicle's movement, especially when turning.

Most of the motors used in EVs are permanent magnet synchronous motor (PMSM)–switch reluctance motor (SRM) or induction motor (IM) with radial or axial flux structures [2, 3]. PMSMs with expensive and rare permanent magnet materials such as SmCo and NdFeB have advantages such as high power and torque density, larger constant power area, less torque ripple [4, 5], and disadvantages such as the high cost of magnets and also the possibility of demagnetization with changes speed is mentioned [6]. In order to improve the performance of PM machines with minimum

cost, ferrite permanent magnets have been proposed as an alternative to expensive permanent magnet materials such as NdFeB and SmCo. For example, in [7, 8] ferrite PM-assisted synchronous reluctance motors with optimal design of the rotor structure are proposed. In [9, 10], electric motors with spoke-type PM rotor to are proposed to increase the volume of the ferrite magnet. In [11], an interesting structure of axial flux motor with segmented rotor is proposed which uses ferrite PMs [11]. The most prominent advantage of SRM motors is the much lower cost compared to PMSM and IM, and on the other hand, it has disadvantages such as low torque density, high torque ripple, high noise, and high vibrations. The use of materials with higher saturation flux density or silicone steel materials as an alternative to Co–Fe has been proposed in [12], which on the other hand has more losses. In [13], by using rigid and nonmagnetic structural stator in slots wedges and reducing the radial vibrations, noise generation has been improved. However, the space required for winding is reduced. Various studies have been done to improve the performance of the squirrel cage induction motors in automotive applications [14]. Squirrel cage induction motors have some advantages such as the robust mechanical structure of the rotor, low cost, low noise and vibration, and no need for particular maintenance [2]. In addition, these motors when fed by variable frequency supply can achieve higher speeds than PMSMs, so the ratio of the maximum speed to the rated speed in squirrel cage induction motors is estimated to be about three [15]. There are various articles reported in the field of multistack axial flux motors regarding design, construction, optimization, and applications [16, 17]. Axial flux motors have special advantages such as a compact structure, proper heat transfer, and more effective usage of active materials, resulting in higher power/torque density [2, 11]. In addition, in the axial flux structures, it is possible to use two rotor discs on the sides of the stator and also assemble the machine to create a multistack structure.

Most of these motors are used in single-drive structures in the form of radial flux, and in multidrive structures, there are both radial flux and axial flux. Axial flux motors are mostly in in-wheel structures or structures with fixed gears. In EVs with a central drive such as ICV, the mechanical differential is responsible for torque distribution and speed regulation between the driving wheels in unequal load conditions. In EVs with more than one propulsion motor, a separate electronic power converter is needed for each motor, and the electric control system or electric differential (ED) is responsible for creating coordination of speed and torque between driving wheels in conditions of speed inequality such as motion on a turning path.

The main purpose of this article is to introduce a dual independent rotor axial flux squirrel cage induction motor (DIR-AFIM) with two degrees of movement freedom for driving each wheel of a vehicle individually. DIR-AFIM is equivalent to two induction motors in series, each of them provides the driving force required for each wheel. This can be implied as a novelty of the new motor in which each rotor owns its individual loading capability. The results illustrated
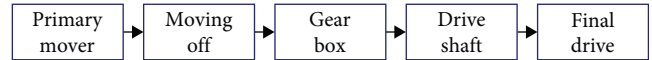

FIGURE 1: Transmission of an automobile power train.

in this paper show that the rotor with greater load values rotates at a higher speed in comparison with the other stator side rotor loaded smaller. This is somewhat similar to the function of the mechanical differential employed in common vehicles. Performance investigation of the proposed motor is carried out through FEM simulations and verified using some experimental measurements on the prototype machine. If employing the proposed machine, without requiring any mechanical differential, only a central power converter and a simple voltage/frequency control are needed. Therefore, with the DIR-AFIM, the cost and complexity of the control system are reduced and the entire power train system has become simpler and more compact.

In section II, the structure of propulsion systems and mechanical transmission of an electric vehicle, as well as the need to use a differential and its role in the vehicle, have been described. In section III, the dynamic calculation of the vehicle in question with the built prototype motor, as well as the vehicle performance and vehicle dynamics equations during lateral motion are stated. In section IV, the mentioned induction motor is introduced, and in the last section, finite element simulations have been performed along with practical results to confirm the correct operation of the vehicle.

2. Powertrain Configuration of Electric Vehicles

Figure 1 shows the powertrain commonly used in vehicles. The final drive, which is the last part of the powertrain, is responsible for the proper distribution of speed, and torque and creating coordination between the wheels. The final drive is the same mechanical differential in single-drive cars, which is replaced by an electric differential in multidrive EVs.

2.1. Mechanical Differential (MD). In many working modes of the vehicle, the driving wheels should have different speeds and torques for the stability of the movement and less wear on the tires. For example, moving in a turning path needs a system that adjusts the proper speed and torque between the driving wheels. In most ICVs, mechanical differential provides this capability. When a vehicle moves in a straight path with equal load torque on both wheels, the pinion and bevel gear in the differential divide the output torque of the drive equally between the two wheels. In this case, the small gears do not rotate around its axis. But when the vehicle turns, it causes the small gears to rotate around its axis and the outer wheel rotates faster. This is a brief explanation of the mechanical differential function and the need to use it. Most single-drive EVs have also used a mechanical differential for this purpose. Figure 2 shows the structure of the basic EVs with a drive. In this structure, the output torque of the gearbox is distributed between the two drive wheels by a mechanical differential (Figure 2(a). In other structures, the electric motor, the fixed gearing, and the
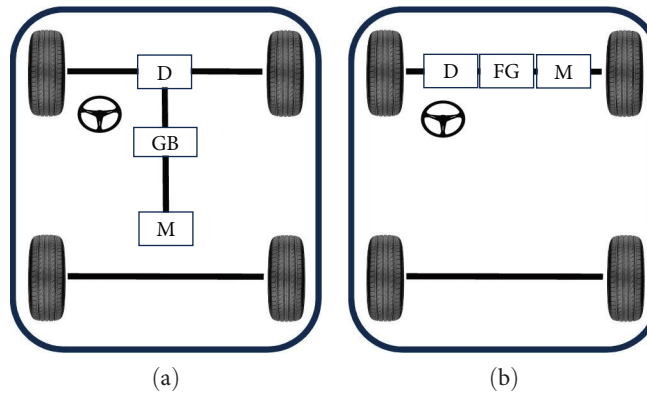
FIGURE 2: EV configuration with MD. (a) With gearbox and (b) with fixed gear and compacted structure.
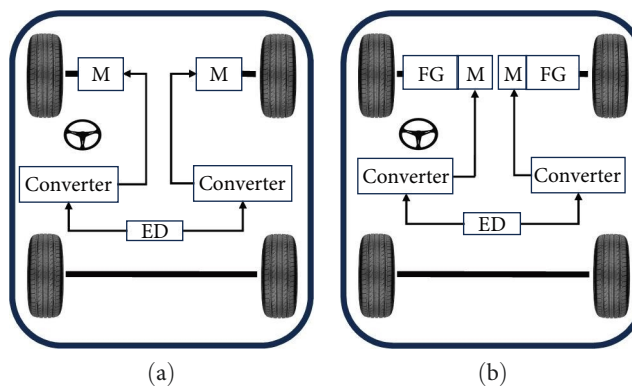

FIGURE 3: EV configuration with ED. (a) Without fixed gear and (b) with fixed gear.

differential can be further integrated into a single assembly while both axles point at both driving wheels (Figure 2(b)). The whole drive train is further simplified and compacted.

2.2. Electrical Differential (ED). In EVs with more than one drive, the electric control system or ED takes the place of the mechanical differential. EVs with two or four drives have outstanding features that improve vehicle stability and provide greater maneuverability for the vehicle when the drive wheels are under uneven road loads [18, 19]. Figure 3 shows some structures with two drivers. In some structures, the motor is connected to the drive wheels with a fixed gear (Figure 3(b)) and in others without a gear (Figure 3(a)). In this case, the motor speed control is equal to the vehicle speed control. In these structures, a separate electronic power converter is needed for each drive. Electric differential produces reference signals for converters based on different control methods and according to its input signals. Finally, the speed and torque of the driving wheels are adjusted to the desired value. For example, in one of the methods, using the direct torque control (DTC) method for two inverters and measuring the speeds of the two driving wheels and comparing it with the input reference signals (steering wheel angle and accelerator pedal), the reference signals required for each converter to adjust the speed motors are produced [20]. In another method, the signals of the acceleration pedal

and the steering wheel angle are used as inputs of the control system based on a neural network to create the values of left and right speed reference signals, and then two independent inverters provide a suitable supply for the motors [21]. The motors can be used in these structures both in the form of axial flux and radial flux.

DIR-AFIM is designed and built in such a way that there is a differential process in it [16] and the structure of the EV is like Figure 3(b). In other words, in this structure, there are two induction motors in series, each of them drives a wheel completely independently of each other by a fixed gear. On the other hand, by using a central converter and a simple voltage–frequency control method, coordination of speed and torque between driving wheels is established. Therefore, the entire power train and control system has become simpler and more compact.

3. Dynamics of the Studied Vehicle

3.1. Tractive Effort and Power Calculation. The components of the resisting force against the longitudinal motion of the vehicle are shown in Figure 4. These forces are rolling resistance (F_r), aerodynamics resistance (F_w), slope resistance (F_g), and acceleration resistance. The total resistance force and the dynamic equation of vehicle motion are expressed as follows [22]:
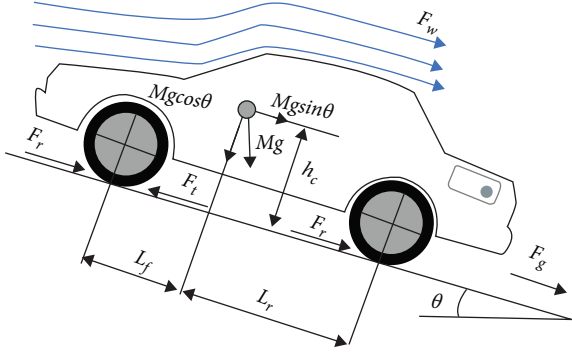
FIGURE 4: Resisting forces in longitudinal motion.

TABLE 1: EV structural parameters.

Parameter	Value
M (kg)	300
g (m/s^2)	9.8
A_f (m^2)	2.0825
C_d	0.5575
λ	1.04
f_r	0.028
i_g	1 : 12
L_f (m)	0.8
η_t (%)	97
h_c (m)	0.5
r_w (m)	0.254
L_r (m)	2
ρ (kg/m^3)	1.225

$$F_{res} = Mgf_r\cos\theta + 0.5\rho A_f C_d(v - v_w)^2 + Mg\sin\theta + M\lambda\frac{dv}{dt}, \tag{1}$$

$$M\lambda\frac{dv}{dt} = F_t - Mgf_r\cos\theta - 0.5\rho A_f C_d(v - v_w)^2 - Mg\sin\theta, \tag{2}$$

where M is the mass of the vehicle, f_r is the coefficient of friction, θ is the road slope, ρ is the air density, A_f is the cross-sectional area, C_d is the shape factor related to the vehicle body, λ is the coefficient of conversion of rotational inertias of rotating components into translational mass, v_w is the wind speed, g is the gravitational constant, v is the vehicle speed and F_t is the total tractive effort.

The total power required (battery output) is:

$$P_{e,in} = \frac{VF_{res}}{\eta_t\eta_m} = \frac{V}{\eta_t\eta_m}\left(Mgf_r\cos\theta + 0.5\rho A_f C_d(v - v_w)^2 + Mg\sin\theta + M\lambda\frac{dv}{dt}\right), \tag{3}$$

where η_t and η_m are the efficiency of the mechanical transmission system and the motor, respectively. Table 1 shows

TABLE 2: Studied EV performance.

Performance	Value
Acceleration time (s)	10
Gradability (deg)	6
Nominal speed (km/hr)	13

the parameter values of Equation (3), which are related to the structure of the EV and suitable for the built prototype [23].

3.2. Studied EV Performance. The operating specifications of the EV is presented in Table 2. The performance of a vehicle is usually described by its maximum cruising speed, gradability, and acceleration. The maximum cruising speed is the maximum constant speed that the car can reach on a flat road. According to the above equations [15]:

$$\frac{T_m i_g \eta_t}{r_w} = Mgf_r\cos\theta + 0.5\rho A_f C_d v^2, \tag{4}$$

where T_m is the torque of the motor, r_w is the wheel radius, and i_g is the gear ratio. gradability is the maximum slope that the vehicle can overcome with a certain constant speed [15]:

$$\frac{T_m i_g \eta_t}{r_w} = Mgf_r\cos\theta + 0.5\rho A_f C_d v^2 + Mg\sin\theta. \tag{5}$$

Acceleration performance is usually defined as the time it takes for the vehicle to reach a certain fixed speed on a flat road from zero speed [15, 24]. From Equation (2):

$$\frac{dv}{dt} = \frac{T_m i_g \eta_t / r_d - Mgf_r\cos\theta - 0.5\rho A_f C_d v^2}{M\lambda}. \tag{6}$$

Then, the acceleration time from speed V_1 to V_2 is obtained as follows:

$$t_a = \int_{v_1}^{v_2} \frac{M\lambda}{T_m i_g \eta_t / r_d - Mgf_r\cos\theta - 0.5\rho A_f C_d v^2}\,dv. \tag{7}$$

3.3. Dynamics of Turning Motion. Turning motion is one of the working regimes of the vehicle and its stability is important during turning. A two-wheel steering two-wheel drive (2WDS-2WS) front-wheel drive vehicle is considered. In the steering mode, when the vehicle has lateral motion, for the stability of the vehicle, the driving wheels need to rotate at different speeds. In this case, the outer wheel of the curve must have a higher angular speed than the inner wheel. Ackerman geometry gives the correct angle of the steering wheel and left and right wheels according to the radius of the turn. At these angles, tire wear reaches its minimum value. Figure 5 shows the correct rotation of the vehicle according to Ackerman's geometry [25, 26]. These equations are:
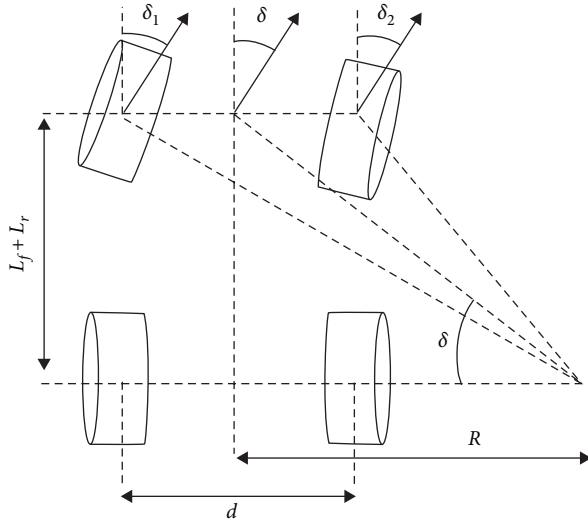
FIGURE 5: Vehicle rotation based on Ackerman geometry.

$$R = \frac{L}{\tan\delta}, \tag{8}$$

$$\tan\delta_1 = \frac{R}{L + d/2}, \tag{9}$$

$$\tan\delta_2 = \frac{R}{L - d/2}, \tag{10}$$

where R is the turning radius, L is the distance between the front and rear axles, d is the lateral distance between the two rear or front wheels, δ is the steering angle, and δ_1 and δ_2 are
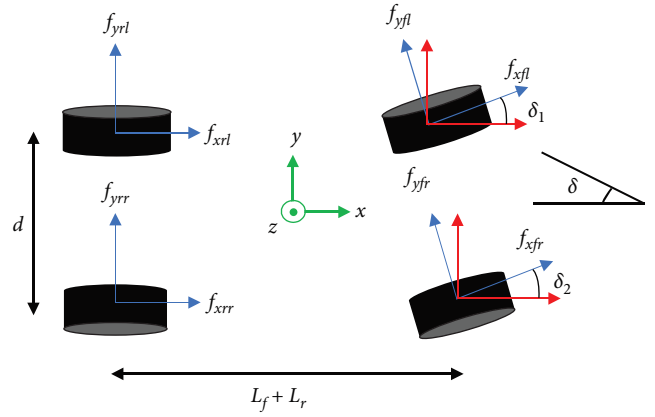

FIGURE 6: The forces on the tire during steering.

the appropriate angle for the left and right wheels to turn right, respectively. When a vehicle has lateral motion, the dynamic equations of the vehicle in linear motion in the x and y directions and the rotational motion of the vehicle around the z-axis are checked. These equations are [27]:

$$m\,\ddot{x} = (F_{xfl} + F_{xfr})\cos(\delta) + (F_{xrl} + F_{xrr}) \\ - (F_{yfl} + F_{yfr})\sin(\delta) + m\dot{\psi}\dot{y}, \tag{11}$$

$$m\,\ddot{y} = (F_{yrl} + F_{yrr}) + (F_{xfl} + F_{xfr})\sin(\delta) \\ + (F_{yfl} + F_{yfr})\cos(\delta) - m\dot{\psi}\dot{x}, \tag{12}$$

$$I_z\ddot{\psi} = L_f(F_{xfl} + F_{xfr})\sin(\delta) + L_f(F_{yfl} + F_{yfr})\cos(\delta) - L_r(F_{yrl} + F_{yrr}) + \frac{d}{2}(F_{xfr} - F_{xfl})\cos(\delta) + \frac{d}{2}(F_{xrr} - F_{xrl}) + \frac{d}{2}(F_{yfl} - F_{yfr})\sin(\delta). \tag{13}$$

In the above relationship, F_y and F_x respectively represent the forces applied in the lateral and longitudinal direction of each tire and the subscripts l,r,f,r respectively represent the left, right, front, and rear, I_z inertia moment of the vehicle, and $\ddot{\psi}$ is its rotational acceleration. The forces applied to each wheel during the lateral motion of the vehicle are shown in Figure 6.

The tire model is needed to obtain F_y and F_x. The well-known Dugoff's model has been used to model tires [28], whose relations are expressed as follows:

$$F_x = C_\sigma \frac{\tau}{1 + \tau} f(\lambda), \tag{14}$$

$$F_y = C_\alpha \frac{\tan\alpha}{1 + \tau} f(\lambda), \tag{15}$$

where

$$\lambda = \frac{\mu F_z(1 + \tau)}{2\left[(C_\sigma\tau)^2 + (C_\alpha\tan\alpha)^2\right]^{1/2}}, \tag{16}$$

$$f(\lambda) = (2 - \lambda)\lambda \text{ if } \lambda < 1, \tag{17}$$

$$f(\lambda) = 1 \text{ if } \lambda > 1. \tag{18}$$

In the above relationships, C_σ and C_α are the tire stiffness parameter and cornering stiffness of the wheel, F_z is the vertical load of the tire, α is the slip angle, τ is the tire slip ratio, and μ is the friction coefficient. The lateral motion of the vehicle causes the load to be transferred to the outside wheel of the turn, and because of this, the normal force distribution of each tire changes. The vertical force relationships for each tire are [28]:
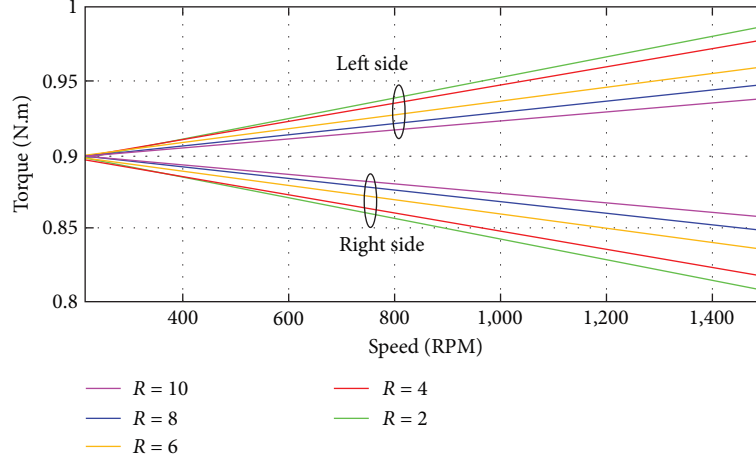
FIGURE 7: Motor-side torque–speed profile on turning path.

$$F_{zfr} = mg\frac{L_r}{2L} + \frac{m_f a_y}{d} - ma_x\frac{h_c}{2L}, \tag{19}$$

$$F_{zfl} = mg\frac{L_r}{2L} - \frac{m_f a_y}{d} - ma_x\frac{h_c}{2L}, \tag{20}$$

$$F_{zrr} = mg\frac{L_f}{2L} + \frac{m_r a_y}{d} + ma_x\frac{h_c}{2L}, \tag{21}$$

$$F_{zrl} = mg\frac{L_f}{2L} - \frac{m_r a_y}{d} + ma_x\frac{h_c}{2L}. \tag{22}$$

In the expression above, L_r is the distance of the rear axle from the center of gravity, L_f is the distance of the front axle from the center of gravity, m_f is the load of the front axle, m_r is the load of the rear axle, d is the lateral distance of the two rear or front wheels, h_c is the distance of the center of gravity from the ground plane, and a_x and a_y are the lateral and longitudinal acceleration of the vehicle, respectively.

According to the above-mentioned equations, the torque–speed characteristic for the driving wheels can be obtained as shown Figure 7. This figure shows torque–speed profile of both rotors corresponding to left and right wheels of the vehicle for different radius of turning to the right in natural steering mode. Small turning radius, higher speed, and sudden steering will cause sudden load transfer to the outer wheel and the vehicle may overturn. The differential system, which is responsible for the proper distribution of the speed between the wheels, determines the vehicle's stability in this situation, and the quick and accurate distribution of the required torque between the wheels improves the vehicle's stability.

4. DIR-AFIM Structure

The proposed motor is a dual rotor axial flux squirrel cage induction motor with a stator in the center. The stator has a two-sided slotted structure and a three-phase full-pitch lap winding for each side. This motor has independent bearings and two degrees of freedom, and all the design steps are described in [16]. Each rotor has 18 aluminum bars and the stator has 24 slots on each side. The number of slots per pole per phase (q) is equal to two and the motor has four magnetic poles. The proposed structure includes a stator in the middle and two rotors on its sides. In this structure, each rotor is able to move individually and fully separated from the other rotor. Therefore, each of the rotors can be loaded with its own particular torque. The movement independence of the rotors can be done by a middle common bearing without requiring mechanical differential. For this purpose, the shaft of one of the rotors is assembled in the inner part of the middle bearing and the shaft of the other rotor is assembled in its outer part. This feature allows each of the rotors to have their own torque and speed, and it is possible to save cost of one bearing and remove the differential system to some extent. Figure 8 shows the 2D and 3D view of the motor simulated in the Ansys Maxwell software, and its electrical and structural parameters are given in Table 3.

This structure is equivalent to two induction motors in series, which are mechanically independent of each other, and the supply voltage is divided between the two motors. This feature causes that when the two rotors have different load torques, with proper voltage and frequency feeding, the required working points can be achieved in the vehicle's rotation mode. In other words, the ability to simultaneously provide more torque and speed in one rotor than the other rotor is only possible by applying the appropriate voltage and frequency by a central inverter for both drive motors in the curved path. No need for any differential or control system to coordinate the speed between the two motors. Figure 9 shows the per phase electrical equivalent circuit of the motor [16].

Also, the speed–torque equation of two motors can be presented as follows [16]:

$$\frac{T_1}{T_2} = \frac{\left(\frac{R'_{r1}}{s_1}\right)\left[\left(\frac{R'_{r2}}{s_2} + R_{th2}\right)^2 + \left(X'_{r2} + X_{th2}\right)^2\right]}{\frac{R'_{r2}}{s_2}\left[\left(\frac{R'_{r1}}{s_1} + R_{th1}\right)^2 + \left(X'_{r1} + X_{th1}\right)^2\right]}. \tag{23}$$

(a)

(b)
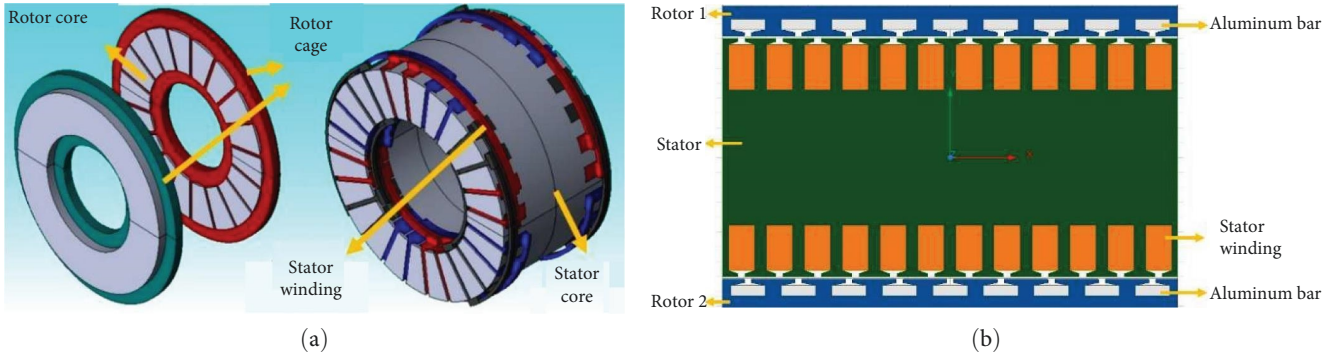
FIGURE 8: Geometry of DIR-AFIM: (a) 3D model and (b) 2D model.

TABLE 3: Motor parameters.

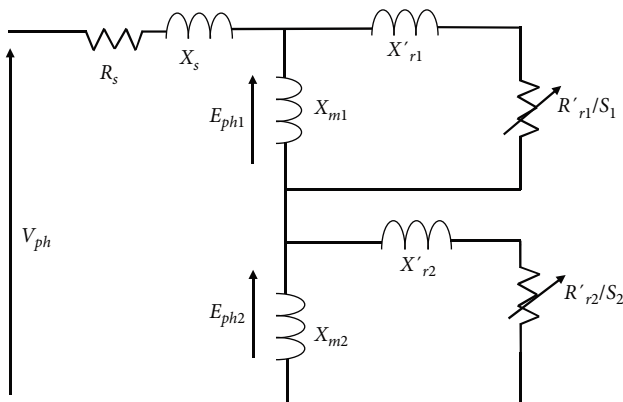| Parameter	Value
Power (kW)	1
Voltage (V)	100
Current (A)	4
Frequency (Hz)	50
Pole number	4
Rotor bars number	18
q	2
$D_{i\ (mm)}$	77.8
$D_{o\ (mm)}$	134.2

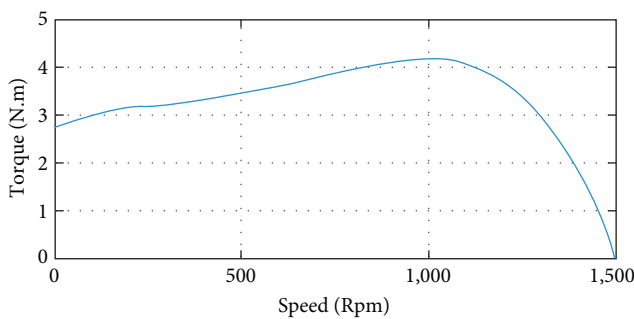FIGURE 9: Electrical equivalent circuit of the motor.

FIGURE 10: Torque–speed curve.

5. Results and Discussion

5.1. FEM Simulations. Finite element simulation of the proposed DIR-AFIM is performed using Ansys Maxwell software, and the characteristics of the proposed propulsion motor is obtained. The torque–speed curve in 100 V 50 Hz power supply is presented in Figure 10. As shown in this figure, the maximum torque is occurs at a speed of about 1,100 rpm and the starting torque is about 2.8 Nm. In the following, by applying the load torque equivalent to the flat path, sloped path, and turning path in three different scenarios, the performance of the DIR-AFIM has been investigated.

When the vehicle is moving in a flat path with equal friction of the drive wheels, both drive wheels have the same load torque and equal speeds. At the beginning of the vehicle's movement, the motor is in the constant torque region with voltage and frequency control to create the starting torque. After reaching the rated voltage and speed, the motor enters the flux weakening area and it is possible to reach higher speeds (about 3.5–4 times the rated speed). At the rated operating point, the motor torque is 1.8 Nm and its speed is 1,404 rpm. According to the gear ratio, the vehicle's torque is 21.6 Nm and its speed is 11 km/hr in steady state. Figure 11 shows the steady state torque of the motor along with the stator current and its harmonic spectrum. Current THD is equal to 8.26% and the amplitude of the fundamental is equal to 3.2 amps. In this case, because both rotors are under the same load torque, the magnetic loading in both air gaps is equal and symmetrical. The color spectrum of the flux density and its vertical component in the air gap is shown in Figure 12.

As Equation (3) shows, the power of the component of the resistive force of inclination and acceleration is a function of speed and its changes. Since the speed coefficient is large in these two components, small speed changes, create large changes in the total power and load resistance force. To optimize the efficiency of the motor, the nominal speed of the vehicle should be reduced as the slope increases. On the other hand, the vehicle should have high acceleration at the starting and low acceleration with the speed increases. These points prevent the production of excess heat and the increase of losses and the motor works with maximum efficiency. At
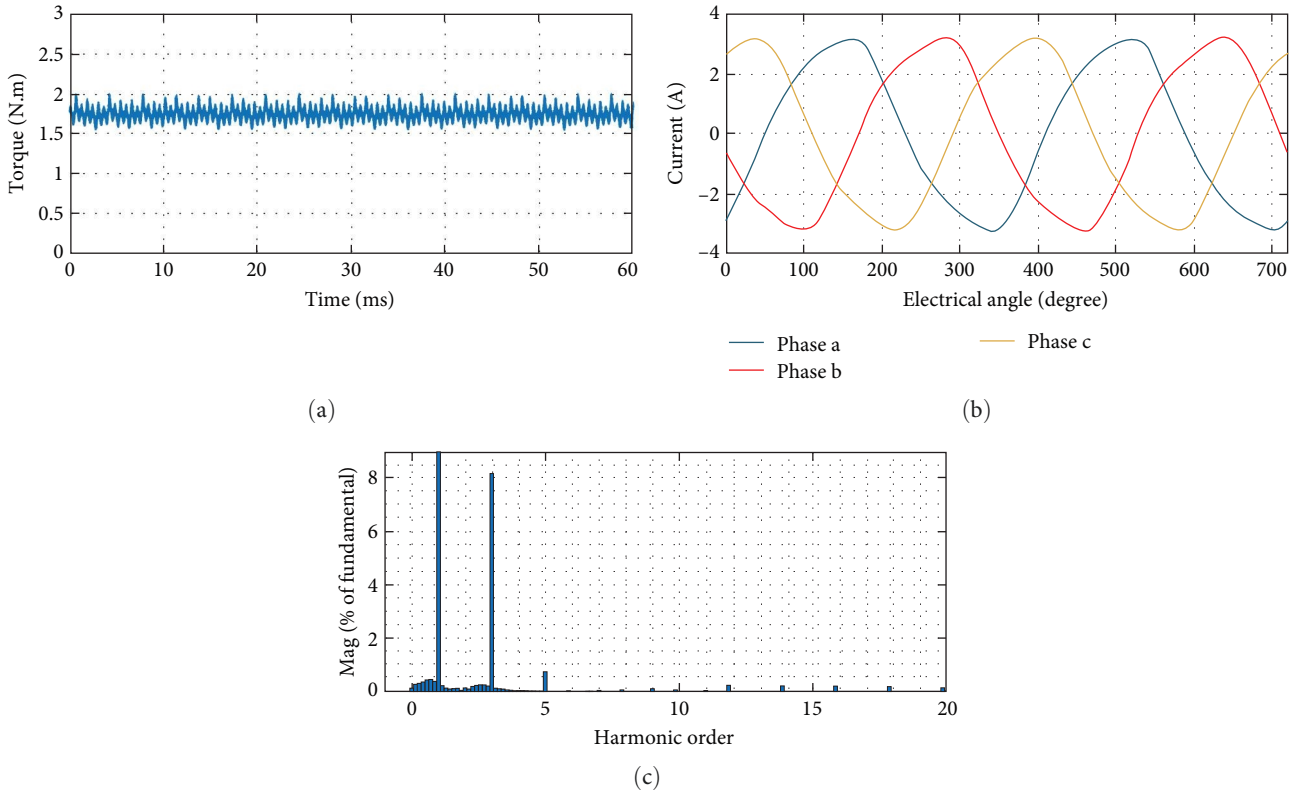
(a)

(b)

(c)

FIGURE 11: Flat path characteristics: (a) motor torque, (b) stator winding current, and (c) harmonic spectrum in 6% slip.
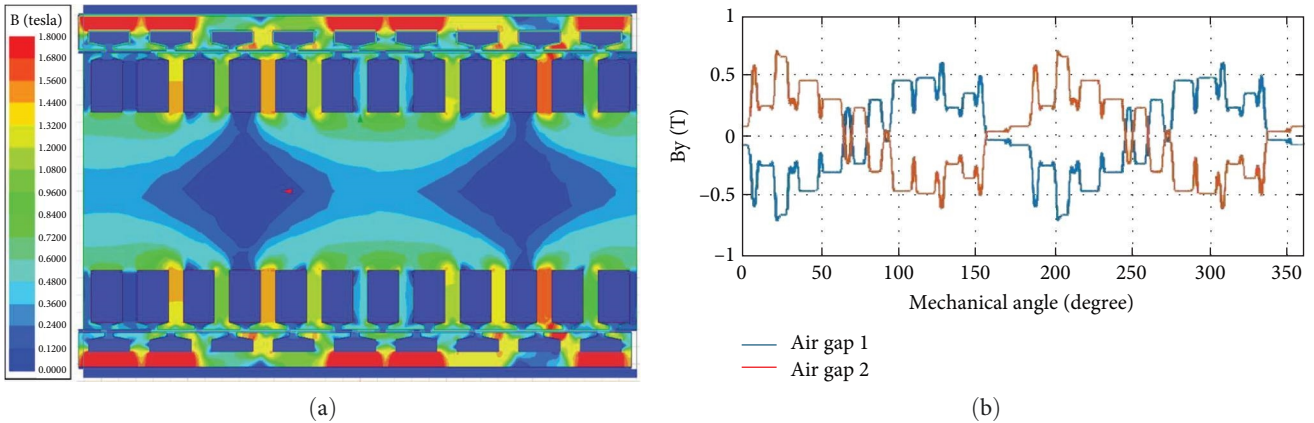

(a)

(b)

FIGURE 12: Flat path flux density: (a) color spectrum and (b) the vertical component of the flux density at air gap (6% slip).

the rated power, the vehicle can navigate a 3-degree slope. In this case, the working point of the motor is near the maximum point of the torque–speed curve. The torque curve along with the current and its harmonic spectrum at 20% slip are shown in Figure 13.

The average torque produced by the motor is about 4 Nm and the slip is 20%. This means that the vehicle's torque is 48 and 27 Nm is for a 3-degree incline compared to the smooth road condition. This indicates that the slope resisting force constitutes a large percentage of the total movement resisting force. Since small induction motors have a larger stable area (larger slip range) than motors with more power, the stator

current is stable at 20% slip and its THD is equal to 4% and the amplitude of its fundamental is equal to 5.455 amps. In this case, the magnetic loading in both air gaps is the same and larger than in the previous case, and the saturation effect of the rotor and stator teeth is evident. The vertical component of the flux density and its color spectrum for 20% slip are shown in Figure 14.

The lateral motion equations were stated in expressions 11, 12, and 13. The two determining factors in the state of the vehicle during lateral motion are the displacement speed and the steering angle, which exist as input signals in most control systems. According to the explanations mentioned in
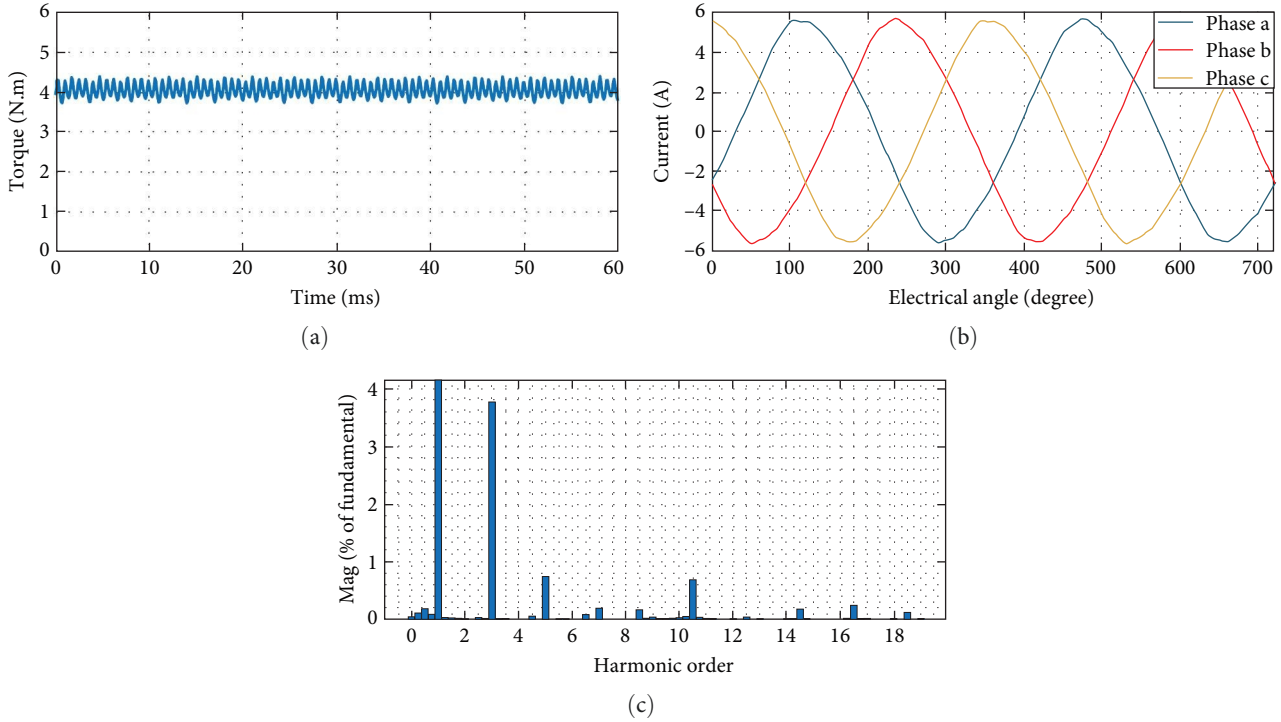
(a)

(b)

(c)

FIGURE 13: Sloped path characteristics: (a) motor torque, (b) stator winding current, and (c) harmonic spectrum in 20% slip.
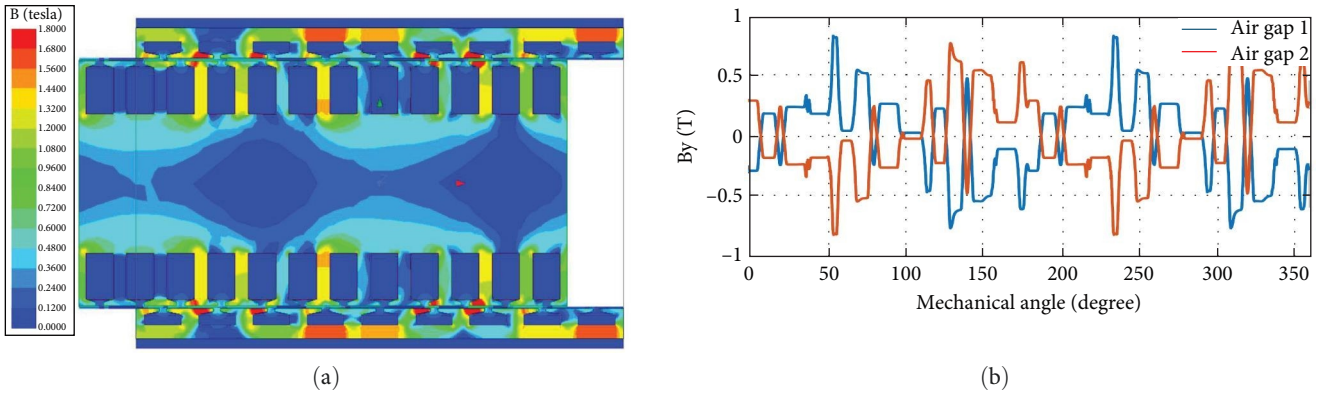

(a)

(b)

FIGURE 14: Sloped path flux density: (a) color spectrum and (b) the vertical component of the flux density at air gap. (20% slip).

section III, when the vehicle is in turning path, the outer wheel of the turn must rotate faster than the inner wheel due to the vehicle's lateral length. On the other hand, the load torque of the outer wheel is greater due to the load transfer from the inner wheel. The desired movement path is as shown in Figure 15, where the vehicle in natural steering mode with a constant speed of 2.5 m/s intends to navigate a 60-degree turn with a radius of 8 m. In this route, the driver slows down before entering the turn. This mode requires a supply voltage equal to 75 V and a frequency of 46 Hz. With these supply values, the torque of the left and right rotors during the turn has been extracted as shown in Figure 16.

From Figure 16 and the gear ratio, the average torque of the left wheel is 12.6 Nm and the right wheel is 9 Nm. On the

other hand, the speed of the left and right driving wheels is another important parameter that guarantees the stability of the vehicle. According to the physics of the problem and the direction of movement, the speed of the left and right wheels should be 2.78 and 2.3 m/s, respectively, so that the vehicle can successfully go around the corner at a speed of 2.5 m/s. This means that the slip of the left and right rotors should be equal to 9% and 25.3%, respectively. Figure 17 shows the current curve of the rotor bars when turning the vehicle, and it can be seen that the frequency of the left and right rotors is 4.14 and 11.67 Hz, respectively. This indicates that the motor has reached the required speeds and the car has completed the turn. In other words, it does not require any differential system, and only by simple control of voltage and
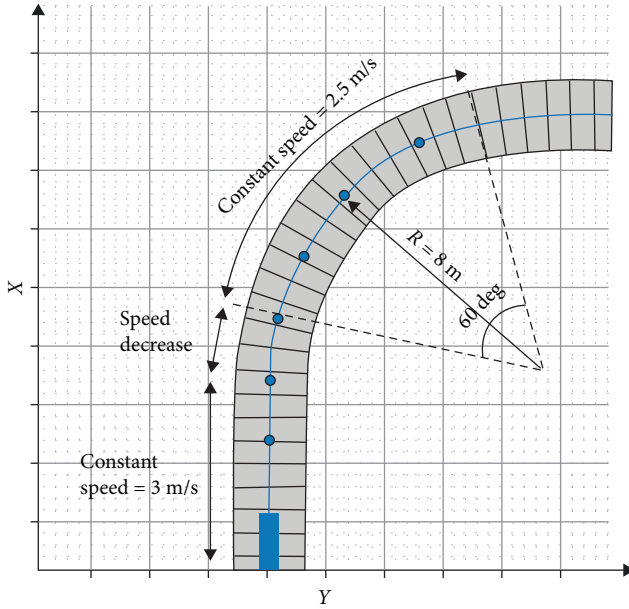
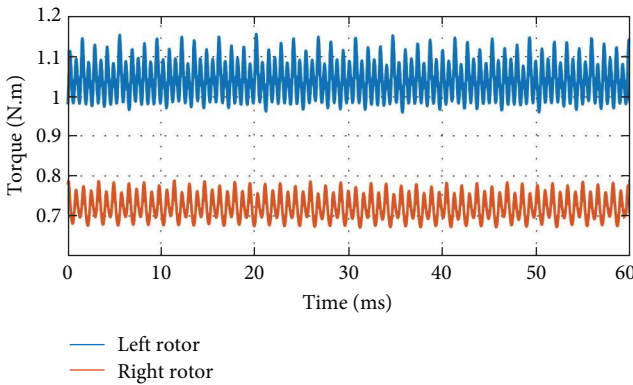FIGURE 15: The studied turning motion path.

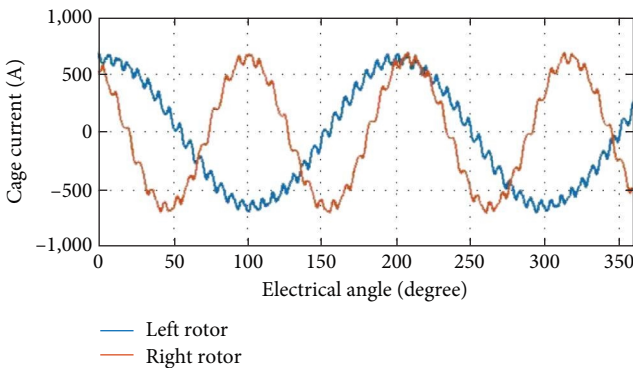FIGURE 16: Left and right rotor torque profiles.

FIGURE 17: Rotor bar currents during turning path.

frequency, the torque and speed required for the vehicle to travel the turning path are provided by the motor. Because the speed is constant during the turn and the steering angle is natural, the voltage and frequency of the converter are
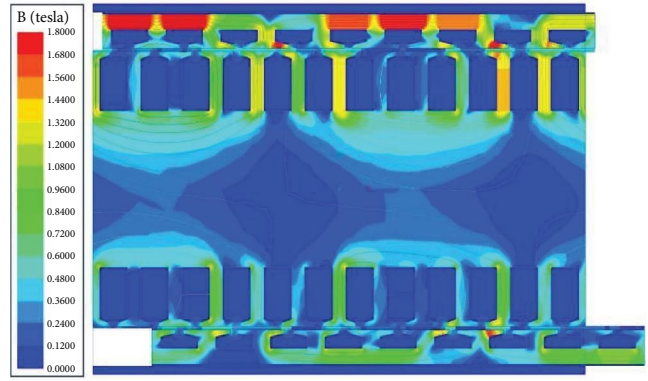

FIGURE 18: The color spectrum of the flux density during the turning path.

unchanged. In this case, the magnetic loading is not symmetrical, and the left rotor (upper rotor in 2D model) has a larger magnetic loading than the right rotor (lower rotor in 2D model). The color spectrum of the flux density is shown in Figure 18.

The stator current and its harmonic spectrum are shown in Figure 19. Considering that in this case the motor is under unequal load torques, the stator current is remain stable. In this case, the THD of stator current is obtained 3.22%, and the current amplitude of fundamental frequency is 3.139 amp. This shows that the motor can perform properly and without disturbance in different and unequal load torques and can play the role of differential well.

5.2. Experimental Results. Figure 20 shows our prototype machine, test bench which includes load applying device, multimeter, and tachometer. Experimental tests are divided into two categories. In the first part, both rotors have equal slips, currents, and speeds. Power factor and efficiency have been measured in steady state. These tests have been performed in 6%, 9%, and 20% slips and the functional quantities obtained by measurements and FEM simulations are presented in Tables 4–6, respectively.

Figures 21 and 22 show the torque–speed and efficiency-speed characteristics, respectively does gathered from FEM simulations and experimental tests. Also, results of 6% and 20% slips corresponding to the operating points of the straight path and the three-degree sloped path, respectively are sown in the Figure 21. As can be seen from this Fig, the simulation results are properly in agreement with the values of the measurements. In the stable working area, the efficiency value varies in the range of 35%–65%, and maximum efficiency occurs in 12.6% slip.

The results show that the stator current values obtained from the measurements (Tables 4–6) in all tests are the little bits smaller than the values obtained from FEM simulations. For example, in a 20% slip, the value of the current obtained from FEM simulations is as fewer 8.8% different from the value obtained from the experimental measurements which shows some accuracies of the simulations.

The second part of the experimental tests is related to the unequal loads applied to the rotors. At first, a torque equal to
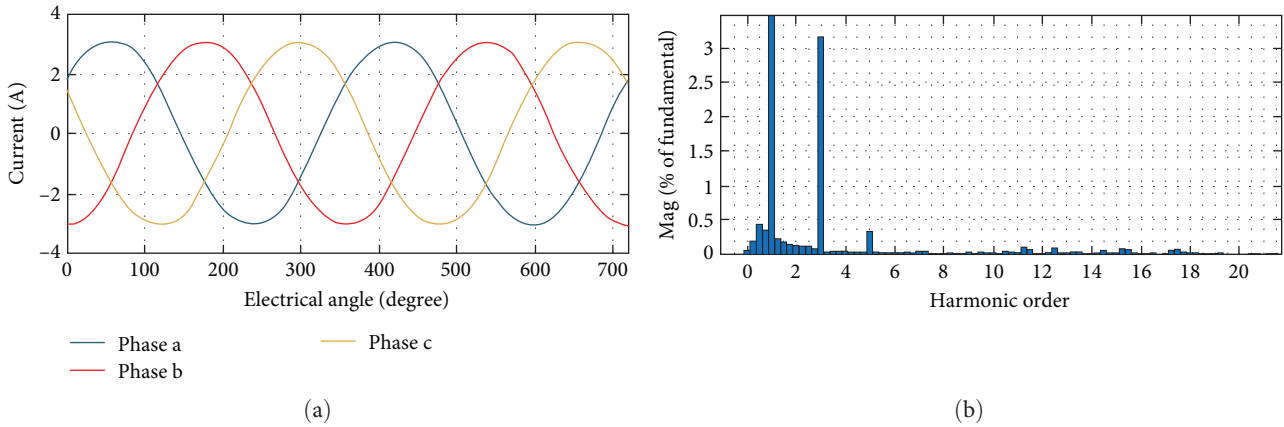
FIGURE 19: Turning path characteristics: (a) stator winding current and (b) harmonic spectrum.
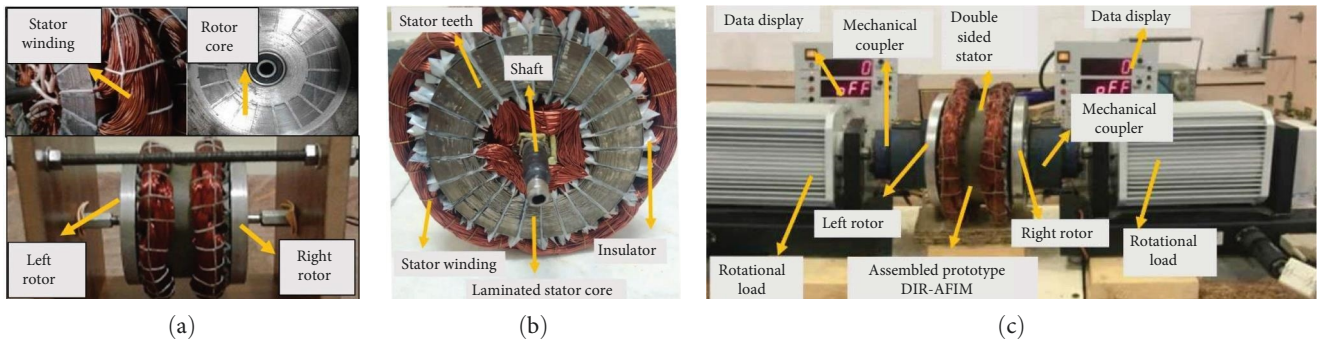

FIGURE 20: (a) Prototype, (b) stator, and (c) experimental setup.

TABLE 4: Experimental results in equal load torque (6% slip).

Parameter	Experimental	Simulation
Voltage (V)	100	100
Current (A)	1.9	2.2
Frequency (Hz)	50	50
Left rotor speed (RPM)	1,420	1,410
Right rotor speed RPM)	1,423	1,409
PF	0.61	0.65
Efficiency	0.53	0.62

TABLE 6: Experimental results in equal load torque (20% slip).

Parameter	Experimental	Simulation
Voltage (V)	100	100
Current (A)	3.1	3.4
Frequency (Hz)	50	50
Left rotor speed (RPM)	1,205	1,200
Right rotor speed (RPM)	1,201	1,198
PF	0.7	0.89
Efficiency	0.51	0.53

TABLE 5: Experimental results in equal load torque (9% slip).

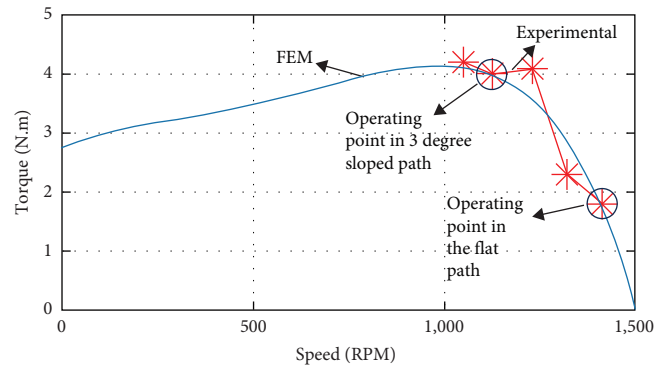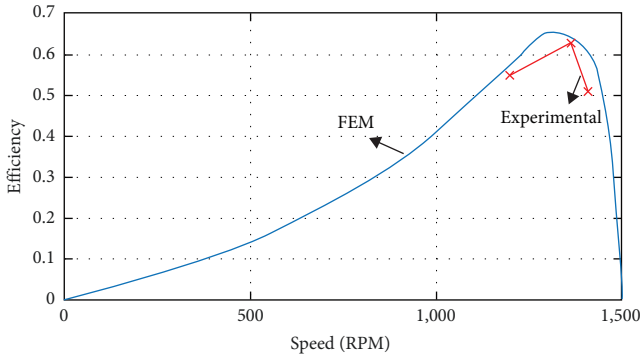| Parameter	Experimental	Simulation
Voltage (V)	100	100
Current (A)	2.1	2.5
Frequency (Hz)	50	50
Left rotor speed (RPM)	1,361	1,365
Right rotor speed (RPM)	1,362	1,363
PF	0.76	0.86
Efficiency	0.61	0.63

FIGURE 21: Torque–speed profile.

FIGURE 22: Efficiency-speed profile.

TABLE 7: Experimental results in unequal load torque (turning to right).

Parameter	Experimental	Simulation
Voltage (V)	70.7	70.7
Current (A)	1.8	2.1
Frequency (Hz)	46	46
Left rotor speed (RPM)	1,260	1,255
Right rotor speed (RPM)	1,040	1,036
PF	0.75	0.8
Efficiency	0.52	0.58

TABLE 8: Experimental results in unequal load torque (turning to left).

Parameter	Experimental	Simulation
Voltage (V)	63	63
Current (A)	1.3	1.6
Frequency (Hz)	48	48
Left rotor speed (RPM)	1,154	1,160
Right rotor speed (RPM)	1,303	1,310
PF	0.7	0.73
Efficiency	0.5	0.55

1 Nm is applied to one of the rotors (say first) and torque of 0.7 Nm to the other rotor (say second). Then, a load equal to 0.75 Nm is applied to the first rotor and 0.5 Nm is applied to the second one. The results of measurement and FEM simulations are given in Tables 7 and 8, respectively for comparison.

The values of the power factor obtained by experimental tests are smaller than the results of the FEM simulations. This issue can be due to the relatively larger air gap of the prototype machine compared to the FEM model caused by assembling tolerances. The first test in unequal load of rotors (Table 7 is equivalent to the vehicle's turning path to the right (third simulation scenario). Similarly, the second test results that shown in Table 8 are corresponding to turning the vehicle to the left. As can be seen in these figures, in certain values of voltage and frequency of power supply, the motor properly responds to the load of the vehicle in the turning path and the measurements confirm the results obtained through FEM simulations with an acceptable accuracy.

6. Conclusion

In this paper, a DIR-AFIM has been proposed as the propulsion system of an electric vehicle, and its desired performance in different working regimes is confirmed through finite element simulations and some experimental measurements. The proposed two-degrees-of-freedom motor with two independent rotors can drive two mechanical loads at the same time. Using the FEM simulations, the proper performance of the motor is examined in three working paths including flat, sloped, and turning paths. The results show that the proposed motor can be suitable for single or two-passenger small-scale vehicles. Although no mechanical or electrical differential is used in this structure, the differential action can be implemented by the self-drive capability of the proposed motor and with a simple frequency and voltage control. Using the simple drive structure of the DIR-AFIM, the complex control systems of electric vehicles can be replaced with a simpler low-cost system. By using the motors with higher power levels, DIR-AFIM can be used in vehicles with better performance.

Data Availability

The data that support the findings of this study are available from the corresponding author upon reasonable request.

Conflicts of Interest

The authors declare no conflict of interest.

Authors' Contributions

Alireza Hesari contributed in the conceptualization, methodology, software, validation, formal analysis, investigation, data curation, writing–original draft preparation, writing–review and editing, and visualization. Ahmad Darabi contributed in the conceptualization, methodology, formal analysis, supervision, project administration, and investigation. Fazel Pourmirzaei Deylami contributed in the conceptualization, methodology, formal analysis, supervision, editing, and investigation.

References

[1] Y. Van Fan, S. Perry, J. J. Klemeš, and C. T. Lee, "A review on air emissions assessment: transportation," *Journal of Cleaner Production*, vol. 194, pp. 673–684, 2018.

[2] Z. Wang, T. W. Ching, S. Huang, H. Wang, and T. Xu, "Challenges faced by electric vehicle motors and their solutions," *IEEE Access*, vol. 9, pp. 5228–5249.

[3] S. Madichetty, S. Mishra, and M. Basu, "New trends in electric motors and selection for electric vehicle propulsion systems," *IET Electrical Systems in Transportation*, vol. 11, no. 3, pp. 186–199, 2021.

[4] Z. Yang, F. Shang, I. P. Brown, and M. Krishnamurthy, "Comparative study of interior permanent magnet, induction, and switched reluctance motor drives for EV and HEV applications," *IEEE Transactions on Transportation Electrification*, vol. 1, no. 3, pp. 245–254, 2015.

[5] G. Pellegrino, A. Vagati, P. Guglielmi, and B. Boazzo, "Performance comparison between surface-mounted and interior PM motor drives for electric vehicle application," *IEEE Transactions on Industrial Electronics*, vol. 59, no. 2, pp. 803–811, 2012.

[6] J. D. Widmer, R. Martin, and M. Kimiabeigi, "Electric vehicle traction motors without rare earth magnets," *Sustainable Materials and Technologies*, vol. 3, pp. 7–13, 2015.

[7] M. De Gennaro, J. Jürgens, A. Zanon et al., "Designing, prototyping and testing of a ferrite permanent magnet assisted synchronous reluctance machine for hybrid and electric vehicles applications," *Sustainable Energy Technologies and Assessments,vol*, vol. 31, pp. 86–101, 2019.

[8] M. Hofer and M. Schrödl, "Investigation of permanent magnet assisted synchronous reluctance machines for traction drives in high power flux weakening operation," in *2020 IEEE Transportation Electrification Conference & Expo (ITEC)*, pp. 335–339, IEEE, Chicago, IL, USA, 2020.

[9] W. Kakihara, M. Takemoto, and S. Ogasawara, "Rotor structure in 50 kW spoke-type interior permanent magnet synchronous motor with ferrite permanent magnets for automotive applications," in *2013 IEEE Energy Conversion Congress and Exposition*, vol. 3, pp. 606–613, IEEE, Denver, CO, USA, 2013.

[10] M. Onsal, B. Cumhur, Y. Demir, E. Yolacan, and M. Aydin, "Rotor design optimization of a new flux-assisted consequent pole spoke-type permanent magnet torque motor for low-speed applications," *IEEE Transactions on Magnetics*, vol. 54, no. 11, pp. 1–5, 2018.

[11] T. Miura, S. Chino, M. Takemoto, S. Ogasawara, A. Chiba, and N. Hoshi, "A ferrite permanent magnet axial gap motor with segmented rotor structure for the next generation hybrid vehicle," in *The XIX International Conference on Electrical Machines —ICEM*, pp. 1–6, IEEE, Rome, Italy, 2010.

[12] K. M. Rahman and S. E. Schulz, "Design of high-efficiency and high-torque-density switched reluctance motor for vehicle propulsion," *IEEE Transactions on Industry Applications*, vol. 38, no. 6, pp. 1500–1507, 2002.

[13] P. O. Rasmussen, J. H. Andreasen, and J. M. Pijanowski, "Structural stator spacers—a solution for noise reduction of switched reluctance motors," *IEEE Transactions on Industry Applications*, vol. 40, no. 2, pp. 574–581, 2004.

[14] M. J. Akhtar and R. K. Behera, "Optimal design of stator and rotor slot of induction motor for electric vehicle applications," *IET Electrical Systems in Transportation*, vol. 9, no. 1, pp. 35–43, 2019.

[15] M. Ehsani, Y. Gao, S. Longo, and K. M. Ebrahimi, *Modern Electric, Hybrid Electric, and Fuel Cell Vehicles*, Taylor & Francis Group, 3rd edition, 2018.

[16] P. Soheili, A. Darabi, and F. P. Deylami, "Design and modeling of a two-degrees-of-freedom dual-rotor axial-flux squirrel cage induction motor," *IET Electric Power Applications*, vol. 17, no. 9, 2023.

[17] F. P. Deylami, A. Darabi, F. Asadi, and A. Gharavi, "Design and performance evaluation of a novel axial-flux hybrid motor with permanent magnet rotor and unpaired damper cage," *IEEE Transactions on Energy Conversion*, vol. 38, no. 2, pp. 1178–1185, 2023.

[18] N. Mutoh and S. Manaka, "Driving performance on low friction coefficient roads which the front-and-rear-wheel-independent-drive-type-electric vehicle (FRID EV)," in *35th Annual Conference of IEEE Industrial Electronics*, pp. 3791–3796, IEEE, 2009.

[19] N. Mutoh, T. Saitoh, K. Natori, and N. Takeda, "Driving force control method for front-and-rear-wheel-independent-drive-type electric vehicles (FRID EVs) effective for safe driving under various road conditions," in *2008 IEEE Vehicle Power and Propulsion Conference*, pp. 1–6, IEEE, Harbin, China, 2008.

[20] B. Tabbache, A. Kheloui, and M. E. H. Benbouzid, "An adaptive electric differential for electric vehicles motion stabilization," *IEEE Transactions on Vehicular Technology*, vol. 60, no. 1, pp. 104–110, 2011.

[21] A. Haddoun, M. E. H. Benbouzid, D. Diallo, R. Abdessemed, J. Ghouili, and K. Srairi, "Modeling, analysis and neural network control of an EV electrical differential," *IEEE Transactions on Industrial Electronics*, vol. 55, no. 6, pp. 2286–2294, 2008.

[22] X. Sun, Z. Shi, G. Lei, Y. Guo, and J. Zhu, "Analysis and design optimization of a permanent magnet synchronous motor for a campus patrol electric vehicle," *IEEE Transactions on Vehicular Technology*, vol. 68, no. 11, pp. 10535–10544, 2019.

[23] N. Murali, S. Ushakumari, V. P. Mini, and A. T. Varghesee, "Sizing and performance analysis of an electric motor in an E-rickshaw," in *2020 IEEE International Conference on Power Systems Technology (POWERCON)*, pp. 1–6, IEEE, Bangalore, India, 2020.

[24] B. Tabbache, A. Kheloui, and M. E. H. Benbouzid, "Design and control of the induction motor propulsion of an electric vehicle," in *2010 IEEE Vehicle Power and Propulsion Conference*, pp. 1–6, IEEE, 2010.

[25] K. Baarath, M. A. Zakaria, and N. A. Zainal, "An investigation on the effect of lateral motion on normal forces acting on each tires for nonholonomic vehicle," in *Intelligent Manufacturing & Mechatronics: Proceedings of Symposium*, pp. 611–621, Springer, Singapore, 2018.

[26] M. Moazen, M. B. B. Sharifian, and M. Sabahi, "Electric differential for an electric vehicle with 4WD/2WS ability," in *24th Iranian Conference on Electrical Engineering (ICEE)*, pp. 751–756,2016, IEEE, Shiraz, Iran, 2016.

[27] L. Chen, Z. Li, J. Yang, and Y. Song, "Lateral stability control of four-wheel-drive electric vehicle based on coordinated control of torque distribution and ESP differential braking," *Actuators*, vol. 10, no. 6, Article ID 135, 2021.

[28] B. Kunjunni, M. A. B. Zakaria, A. P. Majeed, A. A. F. Nasir, M. H. B. Peeie, and U. Z. A. Hamid, "Effect of load distribution on longitudinal and lateral forces acting on each wheel of a compact electric vehicle," *SN Applied Sciences*, vol. 2, pp. 1–8, 2020.